

# Large turbulent reservoirs of cold molecular gas around high-redshift starburst galaxies

E. Falgarone<sup>1</sup>, M. A. Zwaan<sup>2</sup>, B. Godard<sup>1</sup>, E. Bergin<sup>3</sup>, R. J. Ivison<sup>2,4</sup>, P. M. Andreani<sup>2</sup>, F. Bournaud<sup>5</sup>, R. S. Bussmann<sup>6</sup>, D. Elbaz<sup>5</sup>, A. Omont<sup>7</sup>, I. Oteo<sup>4,2</sup> & F. Walter<sup>8</sup>

<sup>1</sup>*LERMA/LRA, Observatoire de Paris, PSL Research University, CNRS, Sorbonne Universités, UPMC Université Paris 06, Ecole normale supérieure, 75005 Paris, France*

<sup>2</sup>*European Southern Observatory, Karl-Schwarzschild-Strasse 2, 85748 Garching, Germany*

<sup>3</sup>*University of Michigan, Ann Arbor, MI, USA*

<sup>4</sup>*Institute for Astronomy, University of Edinburgh, Blackford Hill, Edinburgh EH9 3HJ, UK*

<sup>5</sup>*CEA/AIM, Saclay, France*

<sup>6</sup>*Cornell University, Cornell, NY, USA*

<sup>7</sup>*IAP, CNRS, Sorbonne Universités, UPMC Université Paris 06, 75014 Paris, France*

<sup>8</sup>*Max Planck Institute für Astronomie, Heidelberg, Germany*

**Starburst galaxies at the peak of cosmic star formation<sup>1</sup> are among the most extreme star-forming engines in the universe, producing stars over  $\sim 100$  Myr<sup>2</sup>. The star formation rates of these galaxies, which exceed  $100 M_{\odot}$  per year, require large reservoirs of cold molecular gas<sup>3</sup> to be delivered to their cores, despite strong feedback from stars or active galactic nuclei<sup>4,5</sup>. Starburst galaxies are therefore ideal targets to unravel the critical interplay between this feedback and the growth of a galaxy<sup>6</sup>. The methylidyne cation,  $\text{CH}^+$ , is a most useful molecule for such studies because it cannot form in cold gas without supra-thermal energy input, so its presence highlights dissipation of mechanical energy<sup>7-9</sup> or strong UV irradiation<sup>10,11</sup>. Here, we report the detection of  $\text{CH}^+(J=1-0)$  emission and absorption lines in the spectra of six lensed starburst galaxies<sup>12-15</sup> at redshifts  $z \sim 2.5$ . This line has such a high critical density for excitation that it is emitted only in very dense ( $> 10^5 \text{ cm}^{-3}$ ) gas, and is absorbed in low-density gas. We find that the  $\text{CH}^+$  emission lines, which are broader than  $1000 \text{ km s}^{-1}$ , originate in dense shock waves powered by hot galactic winds. The  $\text{CH}^+$  absorption lines reveal highly turbulent reservoirs of cool ( $T \sim 100 \text{ K}$ ), low-density gas, extending far outside ( $> 10 \text{ kpc}$ ) the starburst cores (radii  $< 1 \text{ kpc}$ ). We show that the galactic winds sustain turbulence in the  $10 \text{ kpc}$ -scale environments of the starburst cores, processing these environments into multi-phase, gravitationally bound reservoirs. However, the mass outflow rates are found to be insufficient to balance the star formation rates. Another mass input is therefore required for these reservoirs, which could be provided by on-going mergers<sup>16</sup> or cold stream accretion<sup>17,18</sup>. Our results suggest that galactic feedback, coupled jointly to turbulence and gravity, extends the starburst phase instead of quenching it.**

Using the Atacama Large Millimeter Array (ALMA), we have detected  $\text{CH}^+(J=1-0)$  lines in high-redshift galaxies: our sample (Table 1) consists of six particularly bright – by virtue of gravitational lensing – submillimeter-selected galaxies (SMGs), with specific star-formation rates  $\gtrsim 3 \times$  those of galaxies on the main sequence<sup>19</sup> at  $z \sim 2$ . The SMGs are extremely compact, with half-

light radii ( $r_{\text{SMG}}$ ) in the range 0.3–1.2 kpc inferred from lens modeling (Table 1). Their rest-frame 360- $\mu\text{m}$  dust continuum images and  $\text{CH}^+(J=1-0)$  spectra are displayed in Figs. 1 and 2. Only the faintest target, SDP130, is not detected in absorption. The peak optical depths at the velocity resolution of  $50 \text{ km s}^{-1}$  are large, in the range 0.25–1.2 (see Methods, Table 2). The absorption lines are broad (mean linewidth  $\Delta v_{\text{abs}} \sim 440 \text{ km s}^{-1}$ ) and three from five are blue-shifted relative to the  $\text{CH}^+$  emission-line centroid ( $v_{\text{em}}$ , Table 2). In the Eyelash, the  $\text{CH}^+$  absorption covers the same velocity range as the OH 119 $\mu\text{m}$  absorption<sup>20</sup>. Three of the  $\text{CH}^+$  emission lines are broader than  $1,000 \text{ km s}^{-1}$  (full width at zero intensity, FWZI  $> 2,500 \text{ km s}^{-1}$ ), far broader than the known CO and  $\text{H}_2\text{O}$  lines of these galaxies<sup>21–23</sup> (Extended Data Table 1). Unlike the absorption lines, these broad emission lines are all centred within  $\sim 30 \text{ km s}^{-1}$  of the known redshift of the SMGs and their width is independent of the star formation rate (Tables 1 and 2).

We detect absorption in five targets, out of the six observed. This high detection rate suggests that the absorbing gas has a quasi-isotropic distribution, a large covering fraction on the SMG dust continuum emission and is a feature common to the starburst phase. The lifetime of the absorbing medium is therefore comparable to that of the starburst phase,  $t_{\text{SMG}} \approx 100 \text{ Myr}$  from SMG samples<sup>2</sup>. The low density gas that is traced by  $\text{CH}^+$  absorption cannot be confined within the starburst cores, because its thermal pressure is orders of magnitude below the high pressure in these  $z \sim 2$  starburst galaxies<sup>24</sup>. We ascribe the absorption linewidths to turbulence (see Methods) with mean turbulent velocity  $\bar{v}_{\text{abs}} = 0.7\Delta v_{\text{abs}}$ .

$\text{CH}^+$  column densities are derived from the absorption line profiles (see Methods, Table 2). The  $\text{CH}^+$  molecules must form in the regions of dissipation of turbulence because, once formed, their lifetime is so short that they cannot be transported. Their abundance is inferred from the turbulent energy flux that sustains the *number* of observed  $\text{CH}^+$  molecules (see Methods). This energy flux depends on the unknown radius  $r_{\text{TR}}$  of the turbulent reservoirs, being proportional to  $\bar{v}_{\text{abs}}^3/r_{\text{TR}}$ . Importantly, in the two targets with enough ancillary data on stellar and gas masses (the Cosmic Eyelash<sup>24</sup> and SDP17b<sup>25</sup>), the mean turbulent velocities are equal to the escape velocities  $v_{\text{esc}}(r) = (2GM_{\text{tot}}/r)^{1/2}$  at radii  $r = 15.6 \text{ kpc}$  and  $22.7 \text{ kpc}$  respectively. Here,  $G$  is the gravitational constant and  $M_{\text{tot}}$  is the sum of the stellar ( $M_*$ ) and gas ( $M_{\text{gas}}$ ) masses. The key provision here is that the associated dynamical times,  $t_{\text{dyn}} = r/\bar{v}_{\text{abs}} = 67$  and  $46 \text{ Myr}$  respectively, are commensurate whereas the stellar masses of these galaxies differ by a factor of 10. We thus adopt  $t_{\text{TR}} \sim 50 \text{ Myr}$  as an approximate age of the observed turbulent reservoirs, and  $r_{\text{TR}} = \bar{v}_{\text{abs}} t_{\text{TR}}$  for their radius. This radius is a lower limit because no dark matter contribution to the total mass  $M_{\text{tot}}$  was assumed. The estimated radii, in the range  $\sim 10$ – $20 \text{ kpc}$  (Table 2), lead to  $\text{CH}^+$  abundances close to those in the Milky Way. The derived masses of the turbulent reservoirs,  $M_{\text{TR}}$ , assuming a radial mean density distribution (see Methods), are  $\approx 0.8$ – $1.4 \times 10^{10} M_{\odot}$  (Table 2). These masses increase the gas mass fraction  $M_{\text{gas}}/M_{\text{tot}}$  by only 10% in the Cosmic Eyelash and SDP17b (see Methods). The kinetic luminosities of the turbulent reservoirs,  $L_{\text{TR}} = \frac{1}{2} M_{\text{TR}} \bar{v}_{\text{abs}}^2/t_{\text{TR}}$  are in the range  $1.2$ – $4.5 \times 10^9 L_{\odot}$  (Table 2).

The broad  $\text{CH}^+$  emission lines trace gas denser than  $\sim 10^5 \text{ cm}^{-3}$  with prodigious velocity dispersions. However, the  $\text{CH}^+$  molecules cannot form in shocks faster than  $\sim 90 \text{ km s}^{-1}$ , otherwise  $\text{H}_2$  (required to form  $\text{CH}^+$ ) would be dissociated<sup>26</sup>. Instead, they must originate in myriad lower velocity shocks that are sufficiently numerous not to be diluted. Irradiated magnetized shocks,

propagating at  $v_{\text{sh}} \sim 40 \text{ km s}^{-1}$  in dense pre-shock gas, are those most efficient at producing  $\text{CH}^+$  (see Methods). The  $\text{CH}^+$  column densities of the shocked gas are high enough to emit lines that are much brighter than those detected, allowing for substantial beam dilution.

The  $\text{CH}^+$  spectra provide considerable insight into the physics of these extreme star-forming systems. Although the sample size is still small, the concomitance of the broad emission and deep absorption lines of  $\text{CH}^+$  suggests that they trace coeval processes, i.e. the dense shocks with high velocity dispersion and the dilute turbulent reservoirs are tied together. Yet, the disparity between the emission and absorption linewidths is striking. The emission linewidths (1100–1400  $\text{km s}^{-1}$ ) in the three sources, the Cosmic Eyelash, G09v1.40 and SDP17b, where they are well determined, are very similar whereas their star formation rates span a factor of  $\sim 5$ . This finding suggests that these lines trace the fast thermal expansion of hot winds at similar temperatures  $T$  in the three sources. For outflow velocities  $v_{\text{out}} \sim \sqrt{3}c_s$ , where  $c_s \sim 500 \text{ km s}^{-1} (\frac{T}{4 \times 10^7 \text{ K}})^{1/2}$  is the sound velocity of the hot wind, the range of observed values,  $v_{\text{out}} = 0.7 \Delta v_{\text{em}} \sim 700\text{--}10^3 \text{ km s}^{-1}$ , provides the range  $T \sim 3\text{--}6 \times 10^7 \text{ K}$  for the hot wind temperature. This high-velocity outflowing hot wind drives large scale shocks in the dense outskirts of the starburst galaxies. Kinetic energy cascades within these shocks down to the velocity of the shocks that are able to form  $\text{CH}^+$ , in a process reminiscent to what is observed in the 35 kpc-long intergalactic shock in the group of galaxies known as Stephan’s Quintet<sup>27</sup>.

The outflowing wind eventually escapes from each galaxy, generating turbulence in its environment. It is this transition to turbulence that causes the outflow momentum to change from mostly outward to random and allows the gas to be re-captured gravitationally. This is why the absorption linewidth in the Eyelash (which is  $10 \times$  less massive than SDP17b) is smaller than in SDP17b. By preventing a fraction of the outflow from escaping the large-scale galaxy potential well, turbulence makes this fraction available for further star formation<sup>28</sup>. Turbulence therefore mitigates the negative feedback of galactic winds on star formation, drawing out the starburst phase.

The  $\text{CH}^+$  molecules that are seen in absorption are observed where they form, i.e. in the turbulent dissipation sites of a  $\sim 100\text{K}$  dilute molecular phase; this suggests that the hot outflows also induce phase transitions in the galaxy environments that could be the giant haloes of neutral hydrogen at  $10^4\text{K}$  detected in  $\text{Ly}\alpha$ <sup>29</sup> at high redshift. Importantly, the mass outflow rates that are required to sustain the kinetic luminosity  $L_{\text{TR}}$  of the turbulent reservoirs closely follow the star formation rates, SFR (see Methods):

$$\dot{M}_{\text{out}} = \frac{0.05 - 0.1}{\eta} \text{SFR} \left( \frac{v_{\text{out}}}{800 \text{ km s}^{-1}} \right)^{-2},$$

$\eta < 1$  being the unknown efficiency of the energy transfer. This is so because the ratios  $L_{\text{TR}}/\text{SFR}$  are observed to be the same within a factor of  $\sim 2$  for all the sources (Tables 1 and 2). If mass loss occurs at  $v_{\text{out}} \sim 700\text{--}10^3 \text{ km s}^{-1}$ , as suggested by the broad emission lines, then the mass outflow rates are probably lower than the star formation rates. Therefore, given their masses, the turbulent reservoirs that are drained by star formation cannot be fed by outflows only. They must be replenished over the lifetime of the starburst by other inflows, from tidal streams of on-going major mergers or from cold stream accretion. The diffuse gas reservoirs result from the mixing of the gas ejected by the starburst-driven outflows with gas present in the wider galaxy environment. By highlighting turbulent dissipation in cool molecular gas,  $\text{CH}^+$  shows that mechanical energy,

fed by gravity and galactic feedback, is largely stored in turbulence and eventually dissipated at low temperature rather than radiated away by hot gas. This turbulent energy storage is observed at two different stages of the feedback process: in the high-velocity dispersion shocked dense gas close to the starburst cores, and very far from them, in the 10kpc-scale massive reservoirs of low-density gas. Turbulence appears to be a key process in the triggering and subsequent regulation of star formation.

**Received: 26 January 2017; Accepted: 21 June 2017.**

**Published online 14 August 2017.**

1. Madau, P. & Dickinson, M. Cosmic Star-Formation History. *ARAstron. Astrophys.* 52, 415–486 (2014)
2. Tacconi, L.J. *et al.* Submillimeter galaxies at  $z \sim 2$ : evidence for major mergers and constraints on lifetimes, IMF and CO-to-H<sub>2</sub> conversion factor. *Astrophys. J.* 680, 246–262 (2008)
3. Carilli, C.L. & Walter, F. Cool Gas in High-Redshift Galaxies. *ARAstron. Astrophys.* 51, 105–161 (2013)
4. Veilleux S., Cecil G. and Bland-Hawthorn, J. Galactic winds. *ARAstron. Astrophys.* 43, 769–826 (2005)
5. Förster Schreiber, N.M. *et al.* The SINS/zC-SINF survey of  $z \sim 2$  galaxy kinematics: evidence for powerful active galactic nucleus-driven nuclear outflows in massive star-forming galaxies. *Astrophys. J.* 787, 38–51 (2014)
6. Somerville, R. S. & Davé, R. Physical Models of Galaxy Formation in a Cosmological Framework. *ARAstron. Astrophys.* 53, 51–113 (2015)
7. Flower, D. & Pineau des Forêts, G. C-type shocks in the interstellar medium: profiles of CH<sup>+</sup> and CH absorption lines. *Mon. Not. R. Astron. Soc.* 297, 1182–1188 (1998)
8. Lesaffre, P. *et al.* Low-velocity shocks: signatures of turbulent dissipation in diffuse irradiated gas. *Astron. Astrophys.* 550, A106 (2013)
9. Godard, B., Falgarone, E. & Pineau des Forêts, G. Chemical probes of turbulence in the diffuse medium: the TDR model. *Astron. Astrophys.* 570, A27 (2014)
10. Godard, B. & Cernicharo, J. A complete model of CH<sup>+</sup> rotational excitation including radiative and chemical pumping processes. *Astron. Astrophys.* 550, A8 (2013)
11. Falgarone, E. *et al.* Strong CH<sup>+</sup>  $J = 1-0$  emission and absorption in DR21. *Astron. Astrophys.* 518, L118 (2010)
12. Eales, S. *et al.* The *Herschel* ATLAS. *PASP* 122, 499–515 (2010)

13. Negrello, M. *et al.* The Detection of a Population of Submillimeter-Bright, Strongly Lensed Galaxies. *Science* 330, 800–804 (2010)
14. Bussmann, R.S. *et al.* Gravitational Lens Models Based on Submillimeter Array Imaging of *Herschel*-selected Strongly Lensed Sub-millimeter Galaxies at  $z > 1.5$ . *Astrophys. J.* 779, 25–51 (2013)
15. Swinbank, A.M. *et al.* Intense star formation within resolved compact regions in a galaxy at  $z = 2.3$ . *Nature* 464, 733–736 (2010)
16. Engel H. *et al.* Most submillimeter galaxies are major mergers. *Astrophys. J.* 724, 233–243 (2010)
17. Dekel, A. *et al.* Cold streams in early massive hot haloes as the main mode of galaxy formation. *Nature* 457, 451–455 (2009)
18. Narayanan, D. *et al.* The formation of submillimetre-bright galaxies from gas infall over a billion years. *Nature* 525, 496–500 (2015)
19. Schreiber, C. *et al.* The *Herschel* view of the dominant mode of galaxy growth from  $z = 4$  to the present day. *Astron. Astrophys.* 575, A74 (2015)
20. George, R.D. *et al.* *Herschel* reveals a molecular outflow in a  $z = 2.3$  ULIRG. *Mon. Not. R. Astron. Soc.* 442, 1877–1883 (2014)
21. Harris, A.I. *et al.* Blind Detections of CO  $J = 1-0$  in 11 H-ATLAS Galaxies at  $z = 2.1-3.5$  with the GBT/Zpectrometer. *Astrophys. J.* 752, 152–166 (2012)
22. Lupu, R.E. *et al.* Measurements of CO Redshifts with Z-Spec for Lensed Submillimeter Galaxies Discovered in the H-ATLAS Survey. *Astrophys. J.* 757, 135–162(2012)
23. Omont, A. *et al.* H<sub>2</sub>O emission in high- $z$  ultra-luminous infrared galaxies. *Astron. Astrophys.* 551, A115 (2013)
24. Swinbank, A.M. *et al.* The Interstellar Medium in Distant Star-forming Galaxies: Turbulent Pressure, Fragmentation, and Cloud Scaling Relations in a Dense Gas Disk at  $z = 2.3$ . *Astrophys. J.* 742, 11–26 (2011)
25. Negrello, M. *et al.* *Herschel*-ATLAS: deep HST/WFC3 imaging of strongly lensed submillimetre galaxies. *Mon. Not. R. Astron. Soc.* 440, 1999–2012 (2014)
26. Hollenbach, D. and McKee, C.F. Molecule formation and infrared emission in fast interstellar shocks. III. Results for  $J$  shocks in molecular clouds. *Astrophys. J.* 342, 306–336 (1989)
27. Appleton, P.N. *et al.* Shock-enhanced C<sup>+</sup> Emission and the Detection of H<sub>2</sub>O from the Stephan’s Quintet Group-wide Shock Using *Herschel*. *Astrophys. J.* 777, 66–82 (2013)

28. Bouché, N. *et al.* The impact of cold gas accretion above a mass floor on galaxy scaling relations. *Astrophys. J.* 718, 1001–1018 (2010)
29. Borisova, E. *et al.* Ubiquitous Giant Ly $\alpha$  Nebulae around the Brightest Quasars at  $z \sim 3.5$  Revealed with MUSE. *Astrophys. J.* 831, 39–48 (2016)
30. *Planck* Collaboration. *Planck* 2013 results. XVI. Cosmological parameters. *Astron. Astrophys.* 571, A16 (2014)

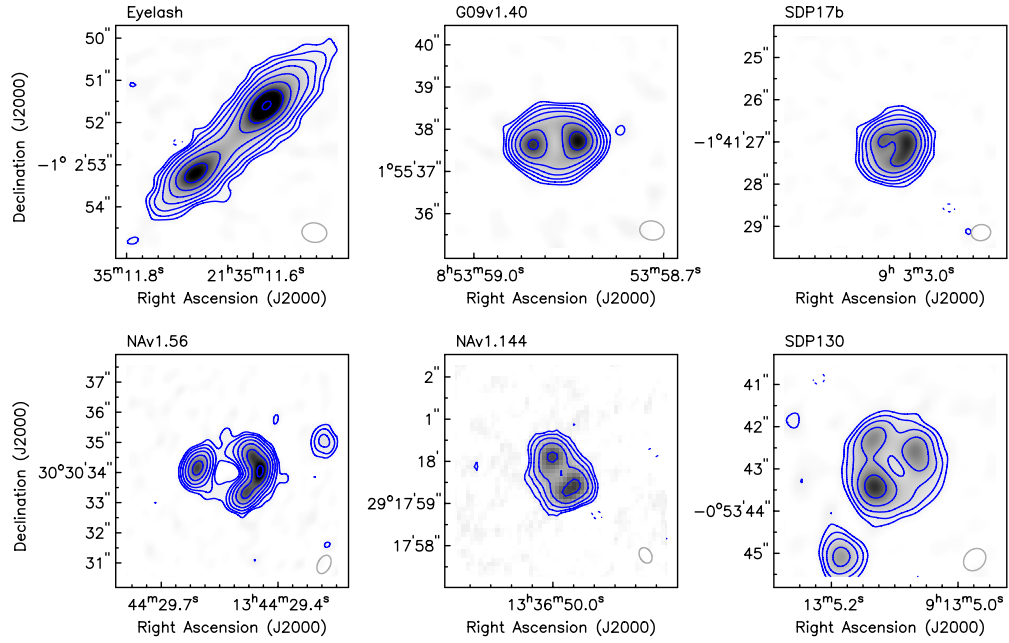


Figure 1: **ALMA rest-frame 360- $\mu\text{m}$  continuum images of our lensed targets.** Solid contours are in steps of  $3\sigma \times 2^n$ ,  $n = 0, 1, 2, \dots$ , and dashed contours at  $-3\sigma$ , where  $\sigma$  is the r.m.s. noise level (Table 1). The synthesised beam is shown in the bottom right corner. In the *Planck* cosmology<sup>30</sup>, 1 arcsec corresponds to 8.4 kpc at  $z = 2.3$  (uncorrected for lensing magnification).

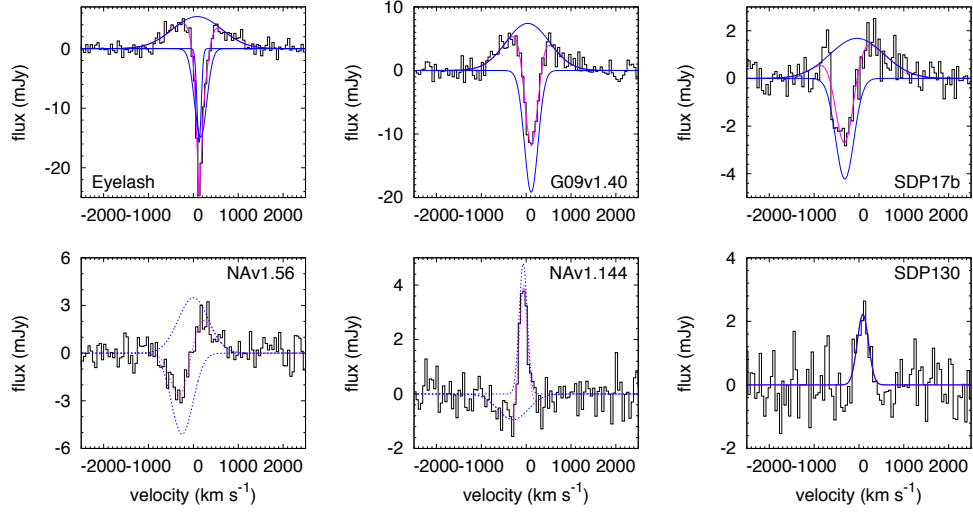


Figure 2: **ALMA  $\text{CH}^+$   $J = 1-0$  spectra of our lensed targets.** Continuum-subtracted  $\text{CH}^+$   $J = 1-0$  spectra, integrated over the solid angle defined in the caption of Table 1. The pink curves show the final fits; the blue curves show the contributions of the emission (one Gaussian) and absorption (one or two Gaussians). The large velocity overlap of the absorption and emission in NAv1.56 and NAv1.144 makes the fits only indicative (dotted lines). The velocity scale is with respect to the accurate redshifts of Extended Data Table 1. The continuum was removed with a linear baseline to perform the fits.



Table 1: Properties of the lensed SMGs and ALMA CH<sup>+</sup> line and continuum fluxes.

Name <sup>a</sup>	$z$ <sup>a</sup>	$\mu$ <sup>b</sup>	$\log L_{\text{FIR}}^c$ L <sub>⊙</sub>	$r_{\text{SMG}}^b$ kpc	SFR <sup>d</sup> M <sub>⊙</sub> yr <sup>-1</sup>	$S_{1.2\text{mm}}$ mJy	$\sigma_{1.2\text{mm}}$ μJy/beam	$S_{\text{CH}^+}^e$ mJy
Eyelash	2.3	~35 <sup>24</sup>	12.22 ± 0.07	~0.3 <sup>f</sup>	285	38.15	30	5.4
G09v1.40	2.0	15.3 ± 3.5 <sup>16</sup>	12.37 ± 0.09	0.41	404	30.12	40	7.4
SDP17b	2.3	6.2 ± 0.2	12.82 ± 0.05	0.72	1133	13.52	30	1.7
NAv1.56	2.3	9.79 ± 0.12	12.87 ± 0.05	0.76	1105	18.73	30	3.5
NAv1.144	2.2	4.16 ± 0.12	12.89 ± 0.08	0.84	1338	18.57	50	> 3.8
SDP130	2.6	8.6 ± 0.4	12.33 ± 0.07	1.2	367	7.4	40	2.

<sup>a</sup> The IAU full names that provide the galactic coordinates of the sources, as well as the full precision redshifts used are given in Extended Table 1. <sup>b</sup> Magnification and half-light size inferred from lens modelling of our ALMA data at rest-frame 360 μm (see Methods), except for G09v1.40 and the Cosmic Eyelash where we adopt values from the literature. The uncertainty on the half-light sizes is ~15%. <sup>c</sup> Intrinsic  $L_{\text{FIR}}$  integrated over 40–120 μm<sup>16</sup>, unlensed with our lens models. <sup>d</sup> Star formation rates assuming a Salpeter initial mass function<sup>16</sup> and no contribution from active galactic nuclei (AGN). These values are intended to illustrate only the differences among the galaxies. <sup>e</sup> Observed peak CH<sup>+</sup> line emission flux integrated over a solid angle defined by the contour level 0.05× the peak continuum level. <sup>f</sup> Size in the source plane of the brightest star-forming region (source X)<sup>24</sup>.

Table 2: Characteristics of the CH<sup>+</sup> lineprofiles and inferred properties of the turbulent reservoirs

Name	$v_{\text{em}}^a$ km s <sup>-1</sup>	$\Delta v_{\text{em}}^a$ km s <sup>-1</sup>	$\Delta v_{\text{abs}}^a$ km s <sup>-1</sup>	$v_{\text{off}}^a$ km s <sup>-1</sup>	$\tau_0^a$	$N(\text{CH}^+)^b$ 10 <sup>14</sup> cm <sup>-2</sup>	$r_{\text{TR}}^c$ kpc	$M_{\text{TR}}^c$ 10 <sup>10</sup> M <sub>⊙</sub>	$L_{\text{TR}}^c$ 10 <sup>9</sup> L <sub>⊙</sub>
Eyelash	30±53	1301±112	232±40	143±11	1.2	8.3	8	1.4	1.2
G09v1.40	28±34	1124±87	361±24	111 ±7	0.70	7.4	12	1.1	2.3
SDP17b	-21±96	1394±157	490±53	-315± 28	0.33	4.7	17	0.9	3.4
NAv1.56	0 <sup>d</sup>	> 814	579 <sup>d</sup>	-249	0.29	4.9	20	0.8	4.5
NAv1.144	0 <sup>d</sup>	> 217	799 <sup>d</sup>	-227	0.25	6.	–	–	–
SDP130	85±21	248±88	–	–	–	–	–	–	–

<sup>a</sup> Parameters inferred from fits made simultaneously on the emission and absorption lines:  $\Delta v_{\text{em}}$  and  $\Delta v_{\text{abs}}$  are the FWHM,  $v_{\text{off}}$  and  $v_{\text{em}}$  are the offset velocity of the absorption Gaussian and the emission line centroid velocity with respect to the systemic velocity of the galaxy as measured in CO, and  $\tau_0$  the absorption peak optical depth (see Methods). <sup>b</sup> Average CH<sup>+</sup> column density in a solid angle subtended by the background source of radius  $r_{\text{SMG}}$  (see Methods). <sup>c</sup> Radius, mass and kinetic luminosity of the turbulent reservoirs computed for  $t_{\text{TR}} = 50$  Myr (see Methods). <sup>d</sup> In these sources, the emission and absorption velocity coverages broadly overlap and the fits have been performed imposing  $v_{\text{em}} = 0$ . In NAv1.56, the convergence of the fit is poor. In NAv1.144, the strong residual emission is so narrow that the fit parameters are non-physical and have not been considered.

**Acknowledgements:** ALMA is a partnership of ESO (representing its member states), NSF (USA) and NINS (Japan), together with NRC (Canada) and NSC and ASIAA (Taiwan), in cooperation with the Republic of Chile. The Joint ALMA Observatory is operated by ESO, AUI/NRAO and NAOJ. NRAO is a facility of the NSF operated under cooperative agreement by Associated Universities, Inc. R.J.I. acknowledges support from ERC in the form of the Advanced Investigator Programme, 321302, COSMICISM. EF and BG acknowledge support from the national CNRS program *Physique et Chimie du Milieu Interstellaire* (PCMI).

**Author contributions:** EF, EB, FB and DE conceived the initial scientific argument and wrote the ALMA proposal with BG, MAZ, PMA, AO and RSB. MAZ reduced the ALMA data. BG and EF analyzed the spectra. BG provided the results of the shock models. RJI, IOG and FW were invited to join the team at a later stage to provide the results of the lens models (IOG) and contribute to a year-long debate on the data interpretation. EF wrote the paper with contributions from all the authors.

**Author informations:** The authors declare that they have no competing financial interests. Correspondence and requests for materials should be addressed to E.F. (email: edith.falgarone@ens.fr).

## Methods

**1 - ALMA observations** The six targets were observed with ALMA in Cycle 2 as part of project 2013.1.00164.S. The  $\text{CH}^+(1-0)$  line ( $\nu_{\text{rest}} = 835.08$  GHz) at redshifts  $z \sim 2.0\text{--}2.6$  is shifted into ALMA band 6 at frequencies between 230 and 270 GHz. The ALMA baseline correlator was configured to use three basebands in the upper sideband, so as to cover a maximum contiguous velocity range of approximately  $5000 \text{ km s}^{-1}$  centred on the  $\text{CH}^+$  line. The low resolution Time Division Mode was used, which, using spectral averaging, provides 240 channels of each 7.812 MHz per baseband. This corresponds to a spectral resolution of  $19 \text{ km s}^{-1}$  after online Hanning smoothing. Between 32 and 34 antennas were used for these observations. A standard observing strategy was used, where a phase reference source was observed every 8 minutes. The total on source time for the six sources combined was 195 minutes. Absolute flux calibration was obtained through the observation of solar system objects and quasars with well-known flux values. The data calibration followed standard routines and was carried out using the CASA 4.4 (common astronomy software applications) package. Continuum images were made for each field using a 'robust' weighting scheme with a Briggs parameter of 0.5. All targets were sufficiently bright to perform one round of phase-only and one round of amplitude and phase self-calibration, which significantly improved the image quality and noise level. These self-calibrated data sets were subsequently used to construct data cubes centred around the redshifted  $\text{CH}^+$  frequency, with a channel spacing of  $50 \text{ km s}^{-1}$ . The typical spatial resolution of the final data cubes is 0.5 arcsec, and the r.m.s. noise level is in the range 0.25 to 0.45 mJy per channel, depending on the data cube.

This paper makes use of the following ALMA data: ADS/JAO.ALMA#2013.1.00164.S.

**2 - Targets** **The Eyelash:** This three-image source strongly lensed by a foreground cluster has a combined amplification of  $37.5^{24}$ . High-resolution interferometry with the Sub-Millimeter Array (SMA) resolved the rest-frame  $260 \mu\text{m}$  continuum emission in two sets of four clumps. The clumps have physical (source-plane) sizes of  $100\text{--}300 \text{ pc}$  in a region  $\sim 2 \text{ kpc}$  within the background galaxy. The total gas mass inferred from CO is  $M_{\text{gas}} \sim 4 \times 10^{10} M_{\odot}$ , the stellar mass is  $M_{\star} = 3 \times 10^{10} M_{\odot}^{24}$ , giving a gas mass fraction  $f_{\text{gas}} = M_{\text{gas}}/(M_{\star} + M_{\text{gas}}) \sim 60\%$ . The CO spectral line energy distribution suggests that this is a multiple component system with different conditions<sup>31</sup>. Low density gas at low temperature is required to model the low-lying transitions of CO. The OH absorption line<sup>20</sup> is interpreted as an outflow originating in the largest star-forming region of the galaxy.

**The H-ATLAS sources:** The redshift determination in G09v1.40 from the  $\text{H}_2\text{O}$  lines<sup>32</sup>,  $z=2.093$ , is different from the centred value<sup>16</sup> of the  $\text{CH}^+$  emission line.  $880 \mu\text{m}$  SMA observation of the dust continuum shows two close components with a separation of  $\sim 1$  arcsec along the east and west direction. The lensing model<sup>16</sup> gives  $\mu = 15.3 \pm 3.5$ . Both the *10m-Keck* telescope and the *Spitzer* space telescope images, in the near-IR and mid-IR respectively, agree about a stellar component magnification of  $\mu = 11.4^{+0.9}_{-1}$ <sup>33</sup>. For all the others, the results of the lensing model applied to our ALMA data (Table 1) differ by  $\sim 20\%$  from those inferred from the SMA data<sup>16</sup>, except for SDP130 where the ALMA-inferred magnification is  $\sim 4\times$  that from SMA. NAv1.56 is a possible merger at a projected separation of  $29 \text{ kpc}$  ( $3.5$  arcsec). In SDP17, the total gas mass inferred from CO is  $M_{\text{gas}} = 5.9 \times 10^{10} M_{\odot}$ , the stellar mass is

$M_* = 2.4 \times 10^{11} M_\odot$ <sup>25</sup>, so that the gas mass fraction  $f_{\text{gas}} \sim 20\%$ .

The IAU names of the targets, redshifts and CO and H<sub>2</sub>O lines characteristics are given in Extended Data Table 1.

**3 - Exploitation of the CH<sup>+</sup> lineprofiles** CH<sup>+</sup> has such a highly endoenergetic formation route via C<sup>+</sup> + H<sub>2</sub> ( $E_{\text{form}} \sim 0.4 \text{ eV}$ ) that a specific chemistry activated by supra-thermal processes is mandatory<sup>7-9</sup>. Its fast destruction due to collisions with H and H<sub>2</sub> makes its lifetime extremely short, even in dilute gas. Being a light hydride with high dipole moment, the critical density of its  $J = 1-0$  transition is  $\sim 10^7 \text{ cm}^{-3}$ , about  $10^4 \times$  larger than that of CO  $J = 1-0$ , so in low-density gas, most molecules are in the ground state providing large  $J = 1-0$  line opacities. In absorption, CH<sup>+</sup> is therefore a tracer of dissipation of mechanical energy in low-density gas ( $n_{\text{H}} < 10^2 \text{ cm}^{-3}$ ). In contrast, in emission, CH<sup>+</sup>  $J = 1-0$  line is a tracer of dense ( $n_{\text{H}} > 10^5 \text{ cm}^{-3}$ ) ultraviolet(UV)-illuminated gas<sup>12</sup>, such as UV-irradiated shocks because, unlike most molecules, the abundance of CH<sup>+</sup> is enhanced in intense UV fields<sup>10,11</sup>.

All our targets are lensed starburst galaxies, with most likely different magnification for the dust continuum emission, the gas seen in absorption and that seen in emission. The angular and spectral resolution of our ALMA data allow some information on the respective distributions of the absorption and the emission in velocity (Extended Data Fig. 1) and of the continuum dust emission and CH<sup>+</sup> absorption and emission in space (Extended Data Figs. 2 and 3). To interpret these data, modelling of differential lensing is warranted. However, the optical depth estimates of the absorption lines are not affected by differential lensing because the background dust emission and the absorbed emission experience the same lensing. Fits have been performed simultaneously on the emission and absorption lines, and the uncertainties on the parameters inferred (Table 2) have been evaluated with the bootstrap method to take into account the correlation between these parameters, in addition to the data noise level. The broad overlap between the absorption and emission velocity ranges makes the uncertainty on the absorption linewidth larger than 100% for NAv1.56. For NAv1.144, no solution with broad emission is found by the fitting procedure, although it is physically plausible.

The emission line luminosities, computed as

$$L_{\text{CH}^+} = 1.04 \times 10^{-3} S_{\text{CH}^+} \Delta v_{\text{em}} \nu_{\text{rest}} D_L^2 / (1 + z)$$

where  $D_L$  is the luminosity distance expressed in Mpc (Extended Data Table 1),  $S_{\text{CH}^+} \Delta v_{\text{em}}$  is the line-integrated flux in  $\text{Jy km s}^{-1}$  and  $\nu_{\text{rest}} = 835.07895 \text{ GHz}$ , are in the range  $2-7 \times 10^8 L_\odot$ . The absorption line optical depth, computed at the velocity  $v_0$  of the absorption peak, is derived from these fits:

$$\tau_0 = -\ln(S_{\text{abs}}(v_0) / [S_{\text{cont}} + S_{\text{em}}(v_0)]),$$

where  $S_{\text{cont}}$ ,  $S_{\text{abs}}$  and  $S_{\text{em}}$  are the continuum, absorption and emission fluxes respectively. The CH<sup>+</sup> column densities are the average values in a solid angle subtended by the area,  $\pi r_{\text{SMG}}^2$ , of the background source assumed to be uniformly covered by the absorbing screen:

$$N(\text{CH}^+) = 3 \times 10^{12} \text{ cm}^{-2} \tau_0 (\Delta v_{\text{abs}} / 1 \text{ km s}^{-1})$$

where  $\Delta v_{\text{abs}}$  is the FWHM of the absorption line.

The formal errors on  $N(\text{CH}^+)$  essentially follow the signal-to-noise ratio of the data. The velocity resolution is coarse and we cannot rule out the possibility that portions of the line might

be saturated. The estimated values of  $N(\text{CH}^+)$  could therefore be lower limits, so in Table 2 we provide them without a compiled error.

**4 - The turbulent framework** Since its discovery in the diffuse interstellar medium (ISM)<sup>34</sup>, the puzzle raised by the large  $\text{CH}^+$  abundances had focused on our Solar Neighbourhood because the line used was an electronic transition ( $\lambda \sim 0.4\mu\text{m}$ ) detected in absorption against nearby stars. The rest frequency of  $\text{CH}^+(J=1-0)$  falling in a domain of high atmospheric opacity, the first observations of  $\text{CH}^+(1-0)$  were achieved with the *Herschel* satellite. The line was detected in absorption against the dust continuum of remote Galactic star-forming regions with *Herschel*/HIFI<sup>11,35,36</sup> and in absorption or emission with *Herschel*/SPIRE<sup>37</sup>. The *Herschel*/HIFI data reveal the large opacity of the  $\text{CH}^+(1-0)$  line in absorption in the Milky Way and show that the  $\text{CH}^+$  absorption profiles differ considerably from those of other lines<sup>36</sup>. The *Herschel*/SPIRE detections in nearby starbursts<sup>38-40</sup> lack spectral resolution to definitely disentangle emission and absorption but Arp220 has a strong absorption line while Mrk231 has the line in emission. A recent detection of the visible lines of  $\text{CH}^+$  against a supernova in M82 reveals a highly turbulent component<sup>41</sup>.

In the Milky Way, the  $\text{CH}^+$  abundances observed in the diffuse molecular gas were found to scale with the turbulent energy transfer rate per unit volume,  $\epsilon$ . The models of turbulent dissipation regions provide an expression of this scaling<sup>9</sup>. In a turbulent cascade, the dissipation rate per unit volume is on average equal to the energy transfer rate per unit volume in the cascade:  $\epsilon_l = \frac{1}{2}\rho_l\bar{v}_l^2/\tau_l$  where  $\tau_l = l/\bar{v}_l$  is the dynamical time of scale  $l$ , and  $\bar{v}_l$  and  $\rho_l$  are the mean velocity and mean mass density at that scale, respectively. It is this quantity,

$$\epsilon_l = \frac{1}{2}\rho_l\bar{v}_l^3/l,$$

that is observed to be uniform on average, albeit with a huge scatter, in the inner Galaxy<sup>42</sup> and is found to be an invariant in numerical simulations of compressible turbulence<sup>43</sup>. This quantity is shortened into "turbulent energy flux" in what follows because it is a flux in the wavenumber-space of the turbulent cascade.

The fraction of the turbulent energy flux required to sustain the observed number of  $\text{CH}^+$  molecules in the volume  $\pi r_{\text{bg}}^2 L$  subtended by the background continuum source (radius  $r_{\text{bg}}$ ) and the length of the line of sight  $L$  is  $\alpha = \dot{E}_{\text{CH}^+}/\dot{E}_{\text{turb}}$ , with

$$\dot{E}_{\text{CH}^+} = N(\text{CH}^+)\pi r_{\text{bg}}^2 E_{\text{form}}/t$$

and

$$\dot{E}_{\text{turb}} = \bar{\epsilon} \times \pi r_{\text{bg}}^2 L.$$

The turbulent energy flux  $\bar{\epsilon}$  is a large scale average and the  $\text{CH}^+$  lifetime is  $t = 1\text{yr} f_{\text{H}_2}^{-1}(n_{\text{H}}/50\text{cm}^{-3})^{-1}$ , where  $f_{\text{H}_2} = 2n(\text{H}_2)/n_{\text{H}}$  is the  $\text{H}_2$  fraction and  $n_{\text{H}}$  and  $n(\text{H}_2)$  are the proton and  $\text{H}_2$  densities, respectively. This is why the  $\text{CH}^+$  opacity of absorption lines that provides  $N(\text{CH}^+)$  is a direct measure of the turbulent energy flux in the medium. Introducing  $N_{\text{H,abs}} = \bar{n}_{\text{H}}L$ , the total column density of gas of average density  $\bar{n}_{\text{H}}$  sampled by the absorption, the observed abundance is  $X(\text{CH}^+) = N(\text{CH}^+)/N_{\text{H,abs}}$ , and therefore  $\alpha =$

$X(\text{CH}^+) \times \bar{n}_{\text{H}}/\bar{\epsilon} \times E_{\text{form}}/t$ . In the Solar Neighbourhood<sup>9</sup>, the average values are  $\langle X(\text{CH}^+) \rangle = 7.6 \times 10^{-9}$ ,  $\bar{n}_{\text{H}} \sim 1 \text{ cm}^{-3}$ , and  $\bar{\epsilon} \sim 10^{-25} \text{ erg cm}^{-3} \text{ s}^{-1}$ , so that  $\alpha = 7.7 \times 10^{-4} f_{\text{H}_2} n_{50}$ , where  $n_{50} = n_{\text{H}}/(50 \text{ cm}^{-3})$  is the local gas density. Galactic observations of [CII] absorption and CI emission along the same background sources where  $\text{CH}^+$  absorption is observed show that this gas is indeed the cold neutral medium (CNM)<sup>44</sup>. The average  $\text{H}_2$  fraction in this low-density molecular gas is found to be  $\bar{f}_{\text{H}_2} = 0.4$  from CH and HF absorption lines along the same sightlines<sup>36</sup>, with a density in the range  $n_{\text{H}} = 30\text{--}50 \text{ cm}^{-3}$ . The filling factor of the CNM in which  $\text{CH}^+$  forms,  $f_v = \bar{n}_{\text{H}}/n_{\text{H}}$ , is much less than unity.

**5 - Determination of the turbulent reservoir properties** We follow the same line of argument to study the turbulent gas around the SMGs. The turbulent approach is supported by the fact that the narrowest [broadest] absorption components have the smallest [largest] velocity offsets ( $v_{\text{off}}$ , Table 2). We also rely on a fundamental property of turbulence – a pencil beam across a turbulent volume samples all the velocities because of the velocity correlations – to relate the size of the turbulent reservoir to the mean turbulent velocity provided by the absorption linewidth. We assume a negligible contribution of rotation to the absorption linewidths (see Extended Data Fig. 1). The unknown  $\text{CH}^+$  abundance is therefore an average value over the volume sampled by the absorption, in the same way as in the Milky Way. We again express that a fraction  $\alpha$  of the turbulent energy flux

$$\dot{E}_{\text{turb}} = \frac{1}{2} M_{\text{abs}} \bar{v}_{\text{abs}}^3 / r_{\text{TR}}$$

in the gas mass sampled by the absorption,  $M_{\text{abs}} = \mu_{\text{p}} m_{\text{H}} N_{\text{H,abs}} \pi r_{\text{SMG}}^2$ , is sufficient to sustain the number of  $\text{CH}^+$  molecules observed in absorption against the background continuum source of radius  $r_{\text{SMG}}$ ,

$$\dot{E}_{\text{CH}^+} = N(\text{CH}^+) \pi r_{\text{SMG}}^2 E_{\text{form}}/t.$$

We thus obtain the relation between the radius of the turbulent reservoir and the  $\text{CH}^+$  abundance:

$$r_{\text{TR}} X(\text{CH}^+) = \alpha \frac{\mu_{\text{p}} m_{\text{H}}}{2} \frac{t}{E_{\text{form}}} \bar{v}_{\text{abs}}^3$$

where the mean turbulent velocity is  $\bar{v}_{\text{abs}} = 0.7 \Delta v_{\text{abs}}$  and  $\mu_{\text{p}}$  is the mean mass per particle.  $\text{CH}^+$  abundances in the range  $(0.8\text{--}5.2) \times 10^{-8}$  follow from the estimated values of  $r_{\text{TR}}$ , and hydrogen column densities in the range  $10^{23}\text{--}9 \times 10^{21} \text{ cm}^{-2}$  are inferred. The mass of the turbulent reservoir is then computed by assuming mass conservation across the different shells, regardless of the global inward/outward or turbulent motions, so that the average density of the reservoir decreases with radius as  $\bar{n}_{\text{H}} \propto r^{-2}$ . As a result, the hydrogen column density at impact parameter  $b$  decreases as  $N_{\text{H}}(b) \propto b^{-1}$  and the mass is  $M_{\text{TR}} = 2\pi \mu_{\text{p}} m_{\text{H}} r_{\text{TR}} r_{\text{SMG}} N_{\text{H,abs}}$ . Introducing  $\Delta v_{400} = \Delta v_{\text{abs}}/(400 \text{ km s}^{-1})$  and  $N_{14} = N(\text{CH}^+)/(10^{14} \text{ cm}^{-2})$  for the observed quantities, so that  $N_{14}/\Delta v_{400} = 12\tau_0$ ,  $X_8 = X(\text{CH}^+)/10^{-8}$  for the inferred abundances,  $\alpha_3 = \alpha/10^{-3}$  and  $t_{50} = t_{\text{TR}}/(50 \text{ Myr})$  for the most probable age of the turbulent reservoirs, with  $t_{\text{TR}} \sim t_{\text{SMG}}/2 \sim 50 \text{ Myr}$ , the radius and mass of the turbulent reservoirs are

$$r_{\text{TR}} = 14.0 \text{ kpc} \times \Delta v_{400} t_{50}$$

and

$$M_{\text{TR}} = 3.8 \times 10^{10} M_{\odot} \times \tau_0 t_{50}^2 r_{\text{SMG,kpc}} (f_{\text{H}_2} n_{50} / \alpha_3)$$

and the  $\text{CH}^+$  abundance is

$$X_8 = 2.5 \Delta v_{400}^2 \alpha_3 / (t_{50} f_{\text{H}_2} n_{50}).$$

A mean mass per particle  $\mu_p = 1.27$  is adopted. These expressions help distinguish the dependence of the inferred sizes and masses on the observed quantities ( $\Delta v_{\text{abs}}$  and  $N_{14}$ ) and free parameters ( $f_{\text{H}_2}$ ,  $n_{50}$  and  $\alpha_3$ ). The local gas density  $n_{50}$  and the  $\text{H}_2$  fraction introduce some degeneracy. However, the range of possible values is limited. From the Galactic studies,  $\bar{f}_{\text{H}_2} = 0.4$  and the gas densities of the  $\text{CH}^+$ -rich regions are in the range  $30 - 50 \text{ cm}^{-3}$ . All of the determinations are therefore within factors of a few. The  $\text{CH}^+$  abundances are close to the Galactic values, as would be expected if the  $\text{CH}^+$  production rate were comparable to that in the Galaxy and the metallicities were similar to solar values, as is observed<sup>45</sup> in star-forming galaxies at  $z \sim 2$ .

The kinetic luminosity is equal to the energy input rate needed to balance the dissipation of the kinetic energy  $E_{\text{turb}} = \frac{1}{2} M_{\text{TR}} \bar{v}_{\text{abs}}^2$  in a dynamical time  $t_{\text{TR}} = r_{\text{TR}} / \bar{v}_{\text{abs}}$  or, with the appropriate units,

$$L_{\text{TR}} = 2.6 \times 10^9 L_{\odot} M_{\text{TR},10} \Delta v_{400}^2 / t_{50},$$

where  $M_{\text{TR},10} = M_{\text{TR}} / (10^{10} M_{\odot})$ . The mass outflow rate at velocity  $v_{\text{out}}$  that is required to balance turbulent dissipation,  $L_{\text{TR}} = \frac{1}{2} \eta \dot{M}_{\text{out}} v_{\text{out}}^2$  (assuming an efficiency  $\eta < 1$  of the energy transfer) is

$$\dot{M}_{\text{out}} \sim \frac{19}{\eta} M_{\odot} \text{ yr}^{-1} L_9 / v_{800}^2$$

where  $L_9 = L_{\text{TR}} / (10^9 L_{\odot})$  and  $v_{800} = v_{\text{out}} / (800 \text{ km s}^{-1})$ .

The turbulent reservoirs are more than 10 times larger the SMGs. Such kpc-scale haloes of low-density gas, comprising a neutral diffuse molecular phase, have been invoked to interpret the low-lying OH absorption lines in Arp 220<sup>46</sup> and NaI D absorption lines<sup>47</sup> in ULIRGs, as well as CO(1-0) lines broader than CO(3-2) lines in distant SMGs<sup>48</sup>. Large kpc-scale haloes of atomic hydrogen are being discovered in the Ly $\alpha$  line around high-redshift galaxies<sup>29,49</sup>. Last, the gas of the turbulent reservoirs is multi-phasic because its average density  $\bar{n}_{\text{TR}} = N_{\text{H,abs}} / r_{\text{TR}} \sim 0.2 - 6 \text{ cm}^{-3}$ , is less than that of the  $\text{CH}^+$ -rich gas at  $n_{\text{H}} \sim 30 - 50 \text{ cm}^{-3}$ , that fills only a low ( $< 10\%$ ) fraction of the volume.

**6 - Models of irradiated shocks** A medium shocked at high velocity emits UV photons that interact with the pre-shock gas<sup>26</sup>. Depending on the shock velocity, this radiative precursor heats, dissociates (for  $v_{\text{sh}} > 90 \text{ km s}^{-1}$ ) or even ionizes (for  $v_{\text{sh}} > 120 \text{ km s}^{-1}$ ) the upstream medium, hence preventing the formation of molecular species. Therefore, while  $\text{CH}^+$  emission has very broad line profiles, it is necessarily formed in shocks of much lower velocity. The extremely broad  $\text{CH}^+$  emission lines trace the large velocity dispersion of lower-velocity shocks, as observed in the kiloparsec-scale shock of the Stephan's Quintet<sup>27,50</sup>.

The production of  $\text{CH}^+$  in low-velocity interstellar shocks has been studied using the Paris-Durham shock code, a state-of-the-art model that was recently improved to take into account



the basic physics of photo-dominated regions<sup>8</sup>. In these starbursts, UV-illumination comes from star formation with a possible contribution from the thermal emission of the optically thick accretion disks of AGNs. Using observations of 22 AGNs<sup>51</sup>, we estimate that the luminosity of a typical AGN with redshift  $z > 1$  is comparable to that due to high-mass star formation, taking dilution within the starburst into account. We ran the code for a range of values of the preshock density ( $10^3 - 10^6 \text{ cm}^{-3}$ ), the UV radiation field ( $1 - 10^4 \times$  the solar neighbourhood value), and the shock velocity ( $10 - 80 \text{ km s}^{-1}$ ), assuming a magnetic field of  $2[n_{\text{H}}/1 \text{ cm}^{-3}]^{1/2} \mu\text{G}$ , and a visible extinction (i.e. shielding from UV photons) of 1 magnitude.

We find that the critical velocity, above which stationary  $C$ -type shocks cannot propagate, strongly depends on the density and the radiation field. Below a critical value ( $v_{\text{sh}} \sim 40 \text{ km s}^{-1}$  i.e.  $C$ -type shocks), the large abundance of  $\text{H}_2$  and the ion-neutral decoupling are sufficient to produce column densities of  $\text{CH}^+$  as large as about  $10^{14} \text{ cm}^{-2}$  in the shock front, within timescales smaller than the expansion timescale of the gas. Above this critical value (i.e.  $J$ -type shocks), the rapid and self-sustained collisional dissociation of  $\text{H}_2$  prevents the immediate formation of  $\text{CH}^+$  in the post-shock where  $\text{H}_2$  reforms and the temperature is still high enough. Column densities of  $\text{CH}^+$  as large as those of  $C$ -type shocks are obtained for a kinetic energy input  $5 \times$  larger, over distances  $100 \times$  larger and for timescales larger than the expansion timescale of the post-shock gas. We conclude that  $J$ -type shocks are far less efficient than  $C$ -type shocks to produce  $\text{CH}^+$ .

Large  $\text{CH}^+$  column densities, up to  $N(\text{CH}^+) \sim 10^{14} \text{ cm}^{-2}$  and spread over several  $\text{km s}^{-1}$  per shock, are formed in  $v_{\text{sh}} = 20 \text{ km s}^{-1}$   $C$ -type shocks propagating in dense pre-shock gas ( $n_{\text{H}} \sim 10^4 \text{ cm}^{-3}$ ). Lines as bright as 1 mJy/beam, estimated in the Large Velocity Gradient approximation<sup>52</sup>, are obtained over a broad range of shock densities  $\geq 10^5 \text{ cm}^{-3}$  and gas temperatures  $\geq 100\text{K}$ . This result does not greatly depend on the gas density. The thickness of each shock is very small, about a few hundred astronomical units. The number of shocks in the beam is difficult to estimate because it depends on the actual geometry of the shock ensemble and its distribution in velocity. Corrected for lensing with the magnifications estimated for the continuum emission, the intrinsic  $\text{CH}^+$  peak brightnesses are about 0.1 mJy/beam. Hence, millions of low-velocity shocks are required in the beam to reproduce the observed  $\text{CH}^+(1-0)$  brightness spread smoothly over  $\sim 1,000 \text{ km s}^{-1}$ . The  $\text{CH}^+(1-0)$  line opacity of individual shocks is less than unity; therefore there is no limitation on the emitted line intensity due to radiative transfer. The lack of detection of  $\text{CO}(1-0)$  lines as broad as the  $\text{CH}^+(1-0)$  lines in those of our targets (except NAv1.56) where  $\text{CO}(1-0)$  has been observed (Extended Data Table 1) is due to the much larger emissivity of the  $\text{CH}^+(1-0)$  transition compared to that of  $\text{CO}(1-0)$ . The Einstein coefficients for spontaneous emission are  $A_{10} = 6.4 \times 10^{-3} \text{ s}^{-1}$  for  $\text{CH}^+(1-0)$ <sup>12</sup> and  $A_{10} = 7.4 \times 10^{-8} \text{ s}^{-1}$  for  $\text{CO}(1-0)$ . For an optically thin line, an upper limit of the  $i \rightarrow j$  line integrated intensity is provided by  $N_i A_{ij} h\nu_{ij}$ , so the  $\text{CO}$  column density in the  $J = 1$  level has to offset the huge ratio  $A_{10}\nu_{10}(\text{CH}^+)/A_{10}\nu_{10}(\text{CO}) \sim 1.6 \times 10^6$ . Therefore as long as the column density of  $\text{CO}$  in the shocks does not exceed that of  $\text{CH}^+$  by a factor of about  $10^7$ , which is the case in the low-velocity  $C$ -type shocks, the  $\text{CO}(1-0)$  line remains very weak and probably below the detection level.

31. Danielson, A.L.R. *et al.*. The properties of the interstellar medium within a star-forming galaxy at  $z=2.3$ . *Mon. Not. R. Astron. Soc.* 410, 1687–1702 (2011)
32. Yang, C. *et al.* Submillimeter  $\text{H}_2\text{O}$  and  $\text{H}_2\text{O}^+$  emission in lensed ultra-luminous infrared galaxies at  $z \sim 2-4$ . *Astron. Astrophys.* 595, A80 (2016)
33. Calanog, J.A. *et al.* Lens Models of *Herschel*-selected Galaxies from High-resolution Near-IR Observations. *Astrophys. J.* 797, 138–164 (2014)
34. Douglas, A.E. & Herzberg G.  $\text{CH}^+$  in interstellar space and in the laboratory. *Astrophys. J.* 94, 381–381 (1941)
35. Falgarone, E. *et al.*  $\text{CH}^+(1-0)$  and  $^{13}\text{CH}^+(1-0)$  absorption lines in the direction of massive star-forming regions. *Astron. Astrophys.* 521, L15 (2010b)
36. Godard, B. *et al.* Comparative study of  $\text{CH}^+$  and  $\text{SH}^+$  absorption lines observed towards distant star-forming regions. *Astron. Astrophys.* 540, A87 (2012)
37. Naylor, D.A. *et al.* First detection of the methylidyne cation ( $\text{CH}^+$ ) fundamental rotational line with the *Herschel*/SPIRE FTS. *Astron. Astrophys.* 518, L117 (2010)
38. van der Werf, P.P. *et al.* Black hole accretion and star formation as drivers of gas excitation and chemistry in Markarian 231. *Astron. Astrophys.* 518, L42 (2010)
39. Spinoglio, L. *et al.* Submillimeter Line Spectrum of the Seyfert Galaxy NGC 1068 from the *Herschel*-SPIRE Fourier Transform Spectrometer. *Astrophys. J.* 758, 108–123 (2012)
40. Rangwala, N. *et al.* Observations of Arp 220 Using *Herschel*-SPIRE: An Unprecedented View of the Molecular Gas in an Extreme Star Formation Environment. *Astrophys. J.* 743, 94–113 (2011)
41. Ritchey, A.M. *et al.* Diffuse Atomic and Molecular Gas in the Interstellar Medium of M82 toward SN 2014J. *Astrophys. J.* 799, 197–212 (2015)
42. Hennebelle P. & Falgarone E. Turbulent molecular clouds. *Astron. Astrophys. Rev* 20, 55–113 (2012)
43. Kritsuk, A.G., Lee, C.T. & Norman, M.L. A supersonic turbulence origin of Larson’s laws. *Mon. Not. R. Astron. Soc.* 436, 3247–3261 (2013)
44. Gerin, M. *et al.* [C II] absorption and emission in the diffuse interstellar medium across the Galactic plane. *Astron. Astrophys.* 573, A30 (2015)
45. Bothwell, M.S. *et al.* Molecular gas as the driver of fundamental galactic relations. *Mon. Not. R. Astron. Soc.* 455, 1156–1170 (2016)
46. Gonzalez-Alfonso E., Smith H.A., Fischer J. & Cernicharo J. The far-infrared spectrum of Arp 220. *Astrophys. J.* 613, 247–261 (2004)

47. Martin, C. Mapping Large-Scale Gaseous Outflows in Ultraluminous Galaxies with Keck II ESI Spectra: Variations in Outflow Velocity with Galactic Mass. *Astrophys. J.* 621, 227–245 (2005)
48. Ivison, R.J. *et al.* Tracing the molecular gas in distant submillimetre galaxies via CO(1-0) imaging with the Expanded Very Large Array. *Mon. Not. R. Astron. Soc.* 412, 1913–1925 (2011)
49. Wisotzki, L., Bacon, R., Blaizot, J. *et al.* Extended Lyman  $\alpha$  haloes around individual high-redshift galaxies revealed by MUSE. *Astron. Astrophys.* 587, A98 (2016)
50. Guillard, P. *et al.* Turbulent Molecular Gas and Star Formation in the Shocked Intergalactic Medium of Stephan’s Quintet. *Astrophys. J.* 749, 158–172 (2012)
51. Shull, J.M., Stevans, M., Danforth, C.W. *HST*-COS observations of AGNs. I. Ultraviolet composite spectra of the ionizing continuum and emission lines. *Astrophys. J.* 752, 162–176 (2012)
52. van der Tak, F.F.S. A computer program for fast non-LTE analysis of interstellar line spectra. *Astron. Astrophys.* 468, 627–635 (2007)
53. Omont, A. *et al.* Observation of H<sub>2</sub>O in a strongly lensed *Herschel*-ATLAS source at  $z = 2.32011$ . *Astron. Astrophys.* 530, L3 (2011)

**Data Availability Statement:** This paper makes use of the following ALMA data: ADS/JAO.ALMA#2013.1.00164.S. The datasets generated and/or analysed during the current study are available in the ALMA archive ([http://almascience.eso.org/aq/?project\\_code=2013.1.00164.S](http://almascience.eso.org/aq/?project_code=2013.1.00164.S)) and are also available from the corresponding author upon reasonable request.

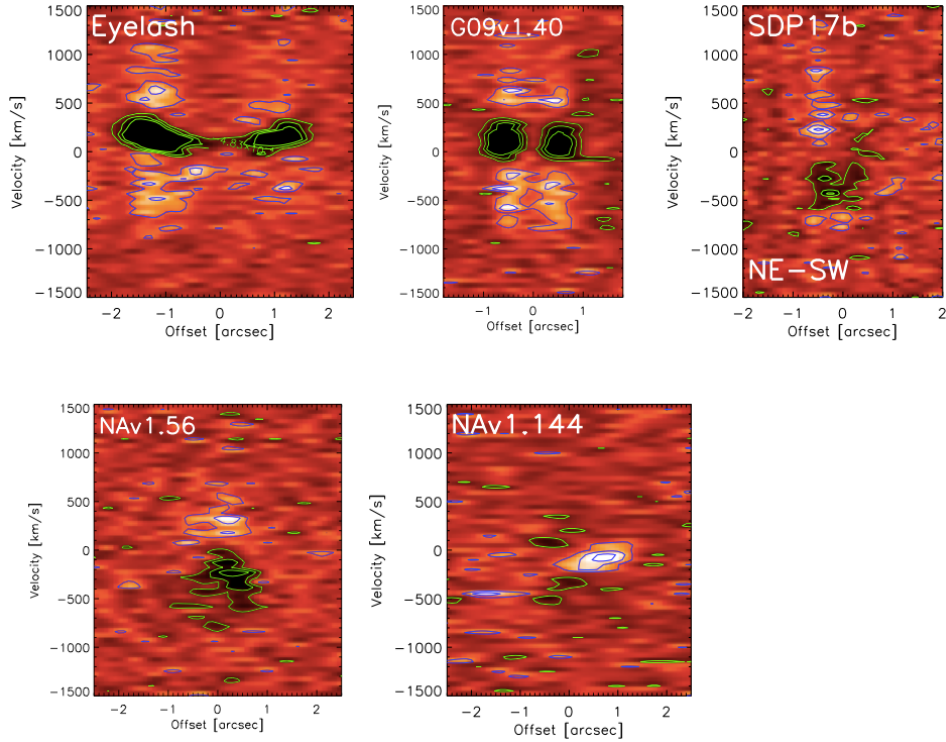
Extended Data Table 1: *Additional properties of the lensed SMGs*

Name	IAU name	$z$	$D_L^a$ Gpc	CO line	$S_{\text{CO}}^c$ Jy km s <sup>-1</sup>	$\Delta v_{\text{CO}}$ km s <sup>-1</sup>	$\Delta v_{\text{H}_2\text{O}}$ km s <sup>-1</sup>
Cosmic Eyelash	SMMJ2135-0102	2.3259	18.95	1-0	2.16±0.11	290± 30	
G09v1.40	J085358.9+015537 <sup>b</sup>	2.0894	16.97	4-3	7.5±2.3	198 ± 51	277±14
SDP17b	J090302.9-014127 <sup>b</sup>	2.3051	18.95	1-0	0.9±0.1	320± 10	250±60 <sup>53</sup>
NAv1.56	J134429.4+303036 <sup>b</sup>	2.3010	18.95	1-0	1.1±0.1	1140±130	593±56 <sup>32</sup>
NAv1.144	J133649.9+291801 <sup>b</sup>	2.2024	17.95	1-0	0.9±0.1	220±20	200±50 <sup>32</sup>
SDP130	J091305.0-005343 <sup>b</sup>	2.6256	21.98	1-0	0.71±0.07	360±40	

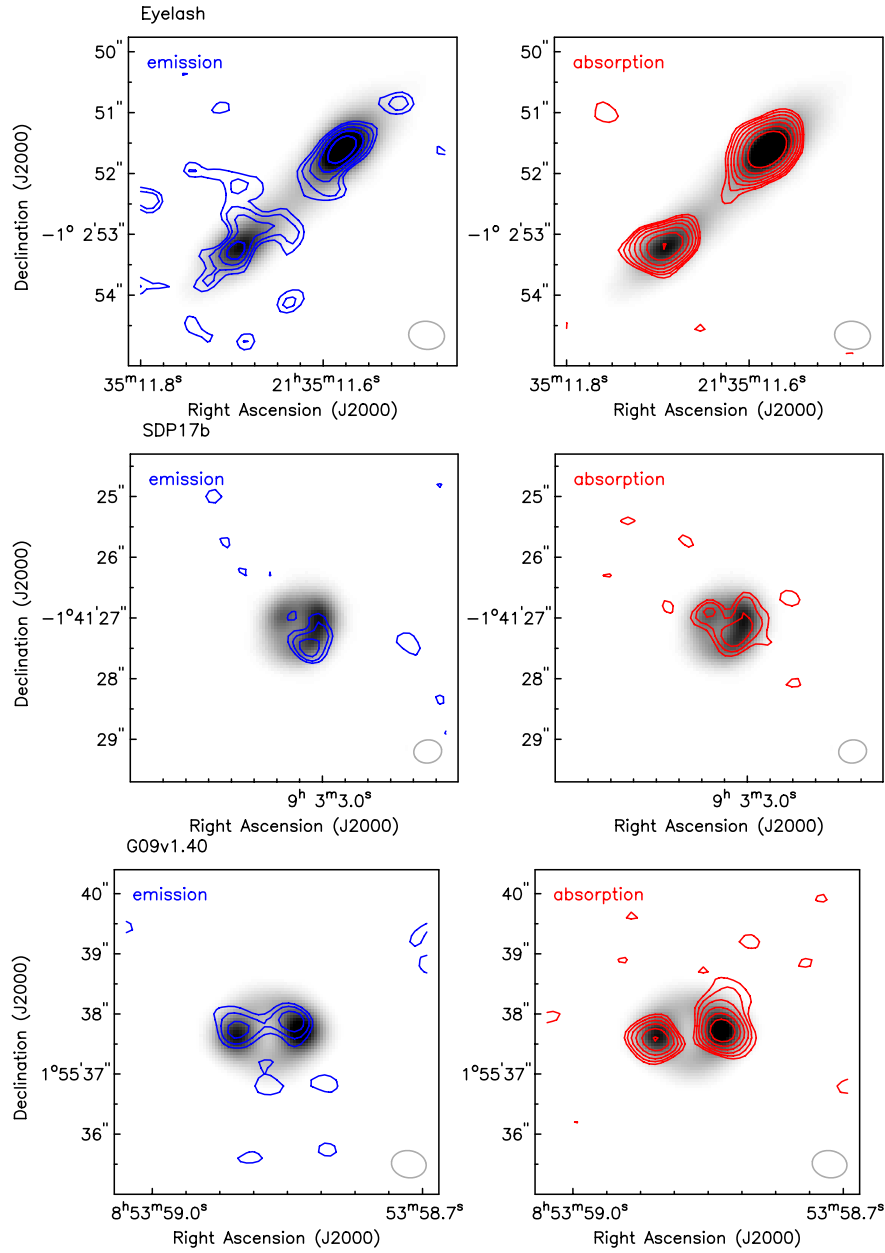
<sup>a</sup> Luminosity distances computed for  $H_0 = 67.3 \text{ km s}^{-1} \text{ Mpc}^{-1}$ ,  $\Omega_M = 0.315$  and  $\Omega_\Lambda = 0.685$ <sup>30</sup>.

<sup>b</sup> *H*-ATLAS sources<sup>12</sup>, redshift determinations<sup>14</sup>

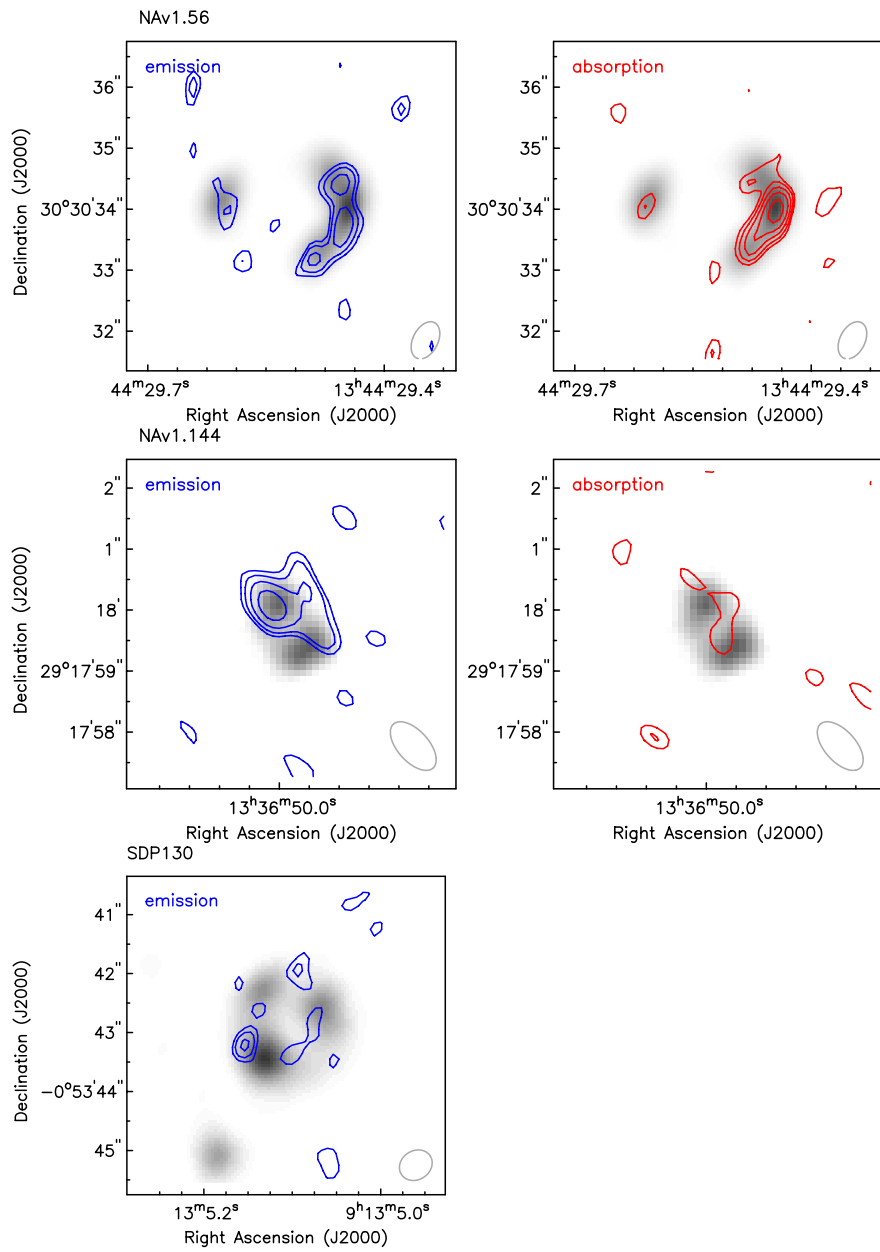
<sup>c</sup> The CO(1-0) results on the *H*-ATLAS sources are from GBT/Zspec observations<sup>21</sup>



Extended Data Figure 1: **Position-velocity diagrams of  $\text{CH}^+$  emission and absorption along selected cuts across the sources.** The cuts are made along East-West directions, except for the Eyelash where it is made along the long-axis of the lensed images and SDP17b where it is along a NE-SW direction.  $\text{CH}^+$  emission appears in white (blue contours) and absorption in black (green contours). The first contour level and steps are  $2\sigma$ . A velocity gradient is seen in the Eyelash absorption, twice smaller than that detected in  $\text{CO}^{24}$ .



Extended Data Figure 2: **CH<sup>+</sup> emission and absorption overlaid on dust continuum emission for the Eyelash, SDP17b and G09v1.40.** The CH<sup>+</sup> line-integrated emission (blue contours) and absorption (red contours), with contour levels in steps of  $2\sigma$ , is overlaid on continuum emission (grey scale). All of the images are lensed, so the differences between the distribution of dust continuum and CH<sup>+</sup> line emission are affected by differential lensing.



Extended Data Figure 3: As in Extended Data Fig.2, but for NAv1.56, NAv1.144 and SDP130. Only emission is detected in SDP130.